Journal of Marine Systems 174 (2017) 106–118

Contents lists available at ScienceDirect

Journal of Marine Systems

journal homepage: www.elsevier.com/locate/jmarsys

Intraseasonal patterns in coastal plankton biomass off central Chile derived from satellite observations and a biochemical model

Fabian A. Gomez [a,b,c,*], Yvette H. Spitz [a], Harold P. Batchelder [d], Marco A. Correa-Ramirez [e]

[a] College of Earth, Ocean, and Atmospheric Sciences, Oregon State University, Corvallis, OR, United States
[b] Department of Coastal Sciences, University of Southern Mississippi, Ocean Springs, MS, United States
[c] Atlantic Oceanographic and Meteorological Laboratory, NOAA, Miami, FL, United States
[d] North Pacific Marine Science Organization (PICES), Sidney, BC, Canada
[e] Instituto de Investigaciones Marinas y Costeras (Invemar), Santa Marta, Colombia

ARTICLE INFO

Article history:
Received 14 June 2016
Accepted 4 May 2017
Available online 05 May 2017

Keywords:
Intraseasonal variability
Coastal upwelling
Plankton composition
central Chile
Humboldt Current System
Madden-Julian Oscillation
Satellite-model comparisons

ABSTRACT

Subseasonal (5–130 days) environmental variability can strongly affect plankton dynamics, but is often overlooked in marine ecology studies. We documented the main subseasonal patterns of plankton biomass in the coastal upwelling system off central Chile, the southern part of the Humboldt System. Subseasonal variability was extracted from temporal patterns in satellite data of wind stress, sea surface temperature, and chlorophyll from the period 2003–2011, and from a realistically forced eddy-resolving physical-biochemical model from 2003 to 2008. Although most of the wind variability occurs at submonthly frequencies (<30 days), we found that the dominant subseasonal pattern of phytoplankton biomass is within the intraseasonal band (30–90 days). The strongest intraseasonal coupling between wind and plankton is in spring-summer, when increased solar radiation enhances the phytoplankton response to upwelling. Biochemical model outputs show intraseasonal shifts in plankton community structure, mainly associated with the large fluctuations in diatom biomass. Diatom biomass peaks near surface during strong upwelling, whereas small phytoplankton biomass peaks at subsurface depths during relaxation or downwelling periods. Strong intraseasonally forced changes in biomass and species composition could strongly impact trophodynamics connections in the ecosystem, including the recruitment of commercially important fish species such as common sardine and anchovy. The wind-driven variability of chlorophyll concentration was connected to mid- and high-latitude atmospheric anomalies, which resemble disturbances with frequencies similar to the tropical Madden-Julian Oscillation.

1. Introduction

Subseasonal variability, here defined as environmental oscillations within the 5 to 130 day band, strongly impacts ocean physical dynamics in Eastern Boundary Upwelling Systems. Large-scale atmospheric disturbances that impact local winds are known to be a main driver of subseasonal variability. Off Oregon, in the northern California Current System, meridional changes in the position of the atmospheric jet stream drive 20-day wind oscillations that determine the dominant fluctuations in coastal upwelling strength during summer (Bane et al., 2007), whereas oscillations with frequencies similar to the tropical Madden Julian Oscillation (MJO; Madden and Julian, 1972) appear to force the near 45 day variability in sea temperature and sea level off central California (Breaker et al., 2001). Intraseasonal (30–90 day) sea surface temperature (SST) variability in the Benguela System is associated with mid-latitude westward-propagating atmospheric disturbances and the Antarctic Oscillation (Goubanova et al., 2013). In the northern Humboldt System, local wind fluctuations, coastal-trapped waves and Rossby waves, the last two triggered by equatorial Kelvin waves, modulate the intraseasonal SST variability (Hormazabal et al., 2001; Bonhomme et al., 2007; Dewitte et al., 2011; Illig et al., 2014). The impact of coastal-trapped and Rossby waves on the Humboldt System decreases southward (Shaffer et al., 1999; Belmadani et al., 2012), while the local wind forcing becomes more important (Hormazabal et al., 2001). Most of the intraseasonal SST variability at Valparaiso (33°S) is explained by local winds (Hormazabal et al., 2001). A coupling between the spatial pattern of SST and the low-level atmospheric jet off central Chile (i.e. the southern Humboldt System) was found at submonthly (<30 days) and intraseasonal frequencies (Renault et al., 2009). Synoptic variability associated with the atmospheric jet appears to be intraseasonally modulated by MJO disturbances (Rahn, 2012), consistent with previous studies suggesting a link between MJO and coastal upwelling (Hormazabal et al., 2002; Rutllant et al., 2004).

* Corresponding author at: Atlantic Oceanographic and Meteorological Laboratory, NOAA, 4301 Rickenbacker Causeway, Miami, FL 33149, United States.
E-mail address: fabian.gomez@noaa.gov (F.A. Gomez).

http://dx.doi.org/10.1016/j.jmarsys.2017.05.003

Although many studies have examined subseasonal physical variability in Eastern Boundary Upwelling Systems, few address the impacts on plankton production. From a theoretical point of view, Botsford et al. (2006) described the impact of subseasonal wind dynamics on plankton production off central California. They found a complicated relation between time-varying upwelling favorable winds and shelf phytoplankton production, as it is dependent on the duration and strength of the upwelling winds, the duration of relaxation (non-upwelling) periods and the shelf width. Bane et al. (2007) linked the north-south changes in the atmospheric jet stream position to subseasonal fluctuations in plankton abundance off Oregon. Recently, Echevin et al. (2014), using a regional ocean model, identified significant intraseasonal variability in plankton production off Peru (north of 14°S), linked to the passage of remotely forced coastal-trapped waves. Less is known about the role of subseasonal dynamics on plankton variability in the southern Humboldt System. Monthly plankton observations from a coastal station off Concepcion (~36.8°S) revealed important intraseasonal changes in the copepod community, linked to upwelling intensity and relaxations (Gonzalez et al., 2015). However, a regional characterization of subseasonal response of phyto- and zooplankton biomass, including description of the dominant spatiotemporal patterns and their connection to large-scale atmospheric features, has not been undertaken off central Chile.

Subseasonal fluctuations in plankton biomass and structure will impact higher trophic levels, such as the early life stages of pelagic fish that rely on plankton production to grow and survive. Fish are especially susceptible to food limitation at the beginning of their exogenous feeding (Cushing, 1990), so subseasonal changes in planktonic prey biomass can impact larval fish early survival and, ultimately, recruitment success. Common sardine (*Strangomera bentinki*) and anchovy (*Engraulis ringens*) are ecologically and commercially important species that live on the shelf, where fluctuations in food may impact their growth and survival. Consequently, it is important to identify locations and periods where the strongest subseasonal fluctuations on plankton biomass occur, and connect those changes to underlying driving factors.

This study characterizes the main subseasonal patterns in plankton biomass off central Chile. We used satellite observations of SST and chlorophyll to identify the dominant subseasonal patterns in coastal upwelling and phytoplankton biomass, and describe their seasonal and interannual changes during 2003–2011. In addition, we used the output of a coupled physical-biochemical ocean model to describe vertical changes in plankton distribution and composition, associated with subseasonal dynamics. The role of MJO disturbances as a driver of the 30-to-90 day plankton variability is also examined.

2. Data and numerical model

2.1. Satellite products

Daily 1 km chlorophyll and SST data from the period 2003–2011 were obtained from level-2 products of the Moderate Resolution Imaging Spectro-radiometer MODIS-Aqua mission (http://oceancolor.gsfc.nasa.gov). The region off central Chile has a relatively high percentage of MODIS cloudless data (>35%), and the temporal gaps at each grid point are usually shorter than 4 days (Morales et al., 2013). Temporal gaps were filled using the Data Interpolating Empirical Orthogonal Function (DINEOF) method, a robust interpolation procedure that is based on an iterative EOF decomposition and preserves time series variance (Beckers and Rixen, 2003). DINEOF does not require extra input parameters, such as signal/noise ratio, anisotropy or minimal number of decompositions, like other methods do. DINEOF has been successfully used in our study region to examine MODIS SST and surface chlorophyll time series variability (Correa-Ramirez et al., 2012). The interpolation was done using a 31-day window for computational convenience, as well as to increase the statistical independence between estimated data in contiguous days. Daily surface wind data with a 0.25° spatial resolution were obtained from the Cross Calibrated Multi-Platform project (CCMP, L3.0; Atlas et al., 2011; https://podaac.jpl.nasa.gov/Cross-Calibrated_Multi-Platform_OceanSurfaceWindVectorAnalyses). CCMP wind stress was derived from CCMP wind speed using the Large and Pond (1981) bulk formulation.

2.2. Numerical model

The Rutgers version of the Regional Ocean Model System (ROMS) (Song and Haidvogel, 1994; Shchepetkin and McWilliams, 2005) was used to simulate the physical dynamics of the upwelling system during the period 2003–2008. The model domain extends from 30.5° to 43°S, and from the coast to 81°W (Fig. 1), with a mean horizontal resolution of 3 km. The 3 km resolution provides realistic representation of mesoscale dynamics over the relatively narrow shelf off Chile, considering that the baroclinic Rossby radius of deformation varies from 34 km at 32°S to 23 km at 43°S, and that the coastal upwelling jet is about 25 km wide. 40 terrain-following vertical layers are arranged to provide enhanced vertical resolution near the surface. Model bathymetry is from the 1 arc degree resolution Smith and Sandwell (1997) version 12.1 bathymetry.

The biochemical model has 8 components: nitrate (NO_3), ammonium (NH_4), small phytoplankton (PS, flagellates and dinoflagellates), large phytoplankton (PL, diatom), small zooplankton (ZS, microzooplankton), large zooplankton (ZL, mesozooplankton), and slow (DS) and fast sinking detritus (DL). The model is parameterized similarly to the North Pacific Ecosystem Model for Understanding Regional Oceanography (NEMURO, Kishi et al., 2007). The differences from Kishi et al. (2007) are the elimination of the silica cycle, dissolved organic nitrogen (DON), and predatory zooplankton in our model. Although silica may limit diatom growth, the observed nitrate-silica ratio off central Chile is usually close to 1 (Anabalon et al., 2007), so

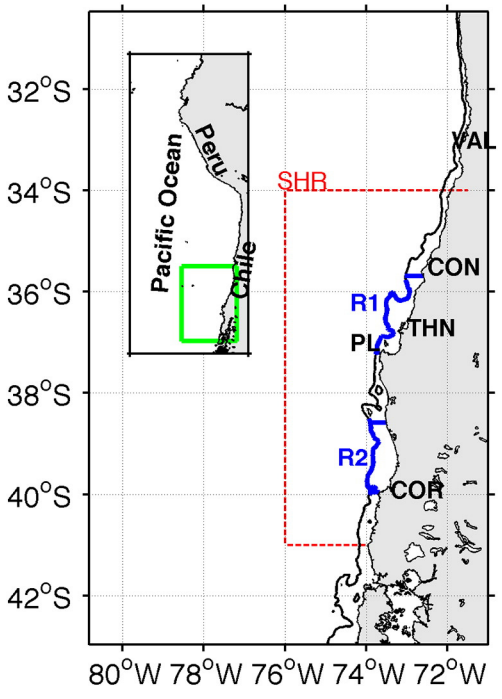

Fig. 1. Full model domain (outermost box). The dashed red lines enclose the southern Humboldt region (SHR) from 34 to 41°S that is examined in the spectral and EOF analysis, and the black contour shows the 200 m isobath. Blue lines depict regions R1 and R2. R1 is used to estimate time series in Fig. 7, and R2 is used to estimate time series in Figs. 7–9. The locations of Valparaiso (VAL), Constitucion (CON), Talcahuano (THN), Point Lavapie (PL), and Corral (COR) are shown. The inset figure shows the Humboldt Current System with the full model domain shown by green lines. (For interpretation of the references to color in this figure legend, the reader is referred to the web version of this article.)

using nitrogen as the only limiting-nutrient for diatom is reasonable. Predatory zooplankton grazing was implicitly incorporated in the mortality rate of diatoms and zooplankton. Non-living particulate organic nitrogen was divided into slow and fast sinking detritus. Slow sinking detritus (DS) consists of the nonliving fraction of phytoplankton and microzooplankton, and microzooplankton egestion. Fast sinking detritus (DL) consists of both the nonliving fraction and egestion of mesozooplankton. Including slow sinking detritus allows nitrogen remineralization in the upper 40–50 m layer, whereas fast sinking detritus exports organic nitrogen to deeper depths. Nitrogen uptake is described by a Michaelis-Menten function, and photosynthesis according to the formulation of Platt et al. (1980). Grazing terms use a Holling type III formulation. All biological rates are temperature dependent. The main biological parameters and their values are given in Table 1.

Table 1
Lower trophic model parameters.

Parameter	Name			Source
	Phytoplankton parameters	PS	PL	
V_{max}	Maximum photosynthetic rate at 0 °C (d^{-1})	0.5	1.0	a,b,c,d
k_{Gpp}	Temperature coefficient for photosynthesis $(°C)^{-1}$	0.0693	0.0693	a
α_P	Initial slope of the P-I curve ($m^2\ W^{-1}$) d^{-1}	0.023	0.028	d,e
β_P	Photoinhibition coefficient ($m^2\ W^{-1}$) d^{-1}	$9 * 10^{-4}$	$4 * 10^{-4}$	d,e
KNO_3	Half saturation constant for nitrate (mmolN m^{-3})	1.0	3.0	a
KNH_4	Half saturation constant for ammonium (mmolN m^{-3})	0.1	0.3	a
ψ_P	Ammonium inhibition coefficient (mmolN $m^{-3})^{-1}$	1.5	3.0	a,c,d
PMor	Mortality at 0 °C (m^3 $mmolN^{-1}$ d^{-1})	0.020	0.020	h
k_{PMor}	Temperature coefficient for mortality $(°C)^{-1}$	0.0531	0.0531	a
PRes	Respiration at 0 °C $(d)^{-1}$	0.03	0.03	a
k_{PRes}	Temperature coefficient for respiration $(°C)^{-1}$	0.0519	0.0519	a
AttP	Light attenuation due to phytoplankton (m^2 $mmolN^{-1}$)	0.0095	0.0095	f
	Zooplankton parameters	ZS	ZL	
GRmPS	Maximum grazing rate at 0 °C on PS (d^{-1})	0.40	0.10	a,b,c
GRmPL	Maximum grazing rate at 0 °C on PL (d^{-1})	0.10	0.30	a,b,c
GRmZS	Maximum grazing rate at 0 °C on ZS (d^{-1})		0.20	a,b,c
k_{Gra}	Temperature coefficient for grazing $(°C)^{-1}$	0.0693	0.0693	a
KPS	Half saturation on PS (mmolN $m^{-3})^2$	0.30	0.8	h
KPL	Half saturation on PL (mmolN $m^{-3})^2$	0.30	0.8	h
KZS	Half saturation on ZS (mmolN $m^{-3})^2$		0.8	h
ZMor	Mortality at 0 °C (m^3 $mmolN^{-1}$ d^{-1})	0.028	0.045	h
k_{ZMor}	Temperature coefficient for mortality $(°C)^{-1}$	0.0531	0.0531	a
α_Z	Assimilation efficiency	0.70	0.70	a
β_Z	Growth efficiency	0.30	0.30	a
	Other parameters			
Nit0	Nitrification rate at 0 °C (d^{-1})	0.07		a,b
k_{Nit}	Temperature coefficient for nitrification $(°C)^{-1}$	0.0693		a
Det2NH4	DS and DL decomposition rate at 0 °C (d^{-1})	0.10		a
K_{D2NH4}	Temperature coefficient for decomposition $(°C)^{-1}$	0.0693		a
wDS	DS sinking rate (m d^{-1})	8		f
wDL	DL sinking rate (m d^{-1})	40		g
Attsw	Light attenuation due to seawater (m^{-1})	0.067		f

PS: small phytoplankton; PL: large phytoplankton; ZS: small zooplankton; ZL: large zooplankton; DS: slow sinking detritus; DL: fast sinking detritus.
[a] Kishi et al. (2007).
[b] Rose et al. (2007).
[c] Yoshie et al. (2007).
[d] Chenillat et al. (2013).
[e] Li et al. (2010).
[f] Spitz et al. (2003).
[g] Fischer and Karakas (2009).
[h] Present study.

Open boundary conditions are Flather for the barotropic velocity (Flather, 1976), Chapman for the free surface (Chapman, 1985), and a combination of radiation and nudging for the baroclinic velocity and passive and biochemical tracers (Marchesiello et al., 2001). The open boundary nudging timescale is 1 day for the incoming signal and 1 year for the outgoing signal. A third order upstream scheme and a fourth order Akima scheme are used for horizontal and vertical momentum advection, respectively. Horizontal viscosity and diffusivity are set to 7 $m^2\ s^{-1}$, increasing gradually to 30 $m^2\ s^{-1}$ in a 100 km wide sponge layer at the open boundaries to reduce signal reflection problems. Mellor and Yamada 2.5-level closure scheme is used for vertical turbulence (Galperin et al., 1988).

Initial and open boundary temperature, salinity and velocities are from the Simple Ocean Data Assimilation (SODA) model (Carton and Giese, 2008). Surface heat flux and wind stress are estimated using bulk parameterization. Daily water flux, air temperature, sea level pressure, humidity, shortwave radiation, and downward longwave radiation are from the European Center for Medium Range Weather Forecast (ECMWF) ERA-Interim reanalysis product (0.75° resolution, Dee et al., 2011). Daily surface wind fields are QuikSCAT winds from the Centre d' Exploitation et de Recherche Satellitaire d' Archivage et de Traitement (CERSAT) products (0.25° resolution). Since QuikSCAT winds are not available in a coastal band ~25 km wide (satellite blind zone), at each latitude the missing coastal grid points were filled with the closest valid observation located west of the coastal band. QuikSCAT and CCMP winds (dataset used in statistical analysis) are highly correlated, as CCMP includes assimilation of the QuikSCAT observations from 1999 to 2009 (Atlas et al., 2011).

Initial and open boundary conditions for the biochemical model components are derived from the Ocean general circulation model For the Earth Simulator (OFES) (Masumoto et al., 2004). OFES results are available only until 2006; therefore, we prescribe the biochemical boundary conditions based on climatological values from OFES during 2007–2008. Because the OFES model only simulates one phytoplankton, one zooplankton and one dissolved inorganic nitrogen pool, we assign 70% (30%) of the phytoplankton to diatoms (small phytoplankton), and 60% (40%) of the zooplankton to mesozooplankton (microzooplankton). This plankton partitioning is based on observed patterns of plankton biomass off central Chile, where diatom and mesozooplankton are the dominant plankton components (Anabalon et al., 2007; Bottjer and Morales, 2007; Escribano et al., 2007). 10% of the phytoplankton biomass is subtracted from the OFES NO_3 pool and assigned to NH_4, which produces a reasonable range of NH_4 values according to reported observations (Tapia et al., 2010). The slow and fast sinking detritus concentrations are assumed to be 10% each of the OFES phytoplankton biomass, and are subtracted from the OFES NO_3 pool. Sensitivity simulations revealed that changes to those allocations do not greatly affect our model results and do not change any of the study findings. A 1-year spin-up was done from January to December of 2002; effects of the initial partitioning conditions vanished during the spin-up period. Boundary conditions, other than NO_3, only weakly influenced plankton biomass beyond an ~100 km wide region on the model domain periphery (i.e. plankton concentrations within the inner domain are mostly determined by local dynamics). After spin-up, the model was run continuously until December of 2008, with daily averaged fields saved. The physical-biochemical model reasonably reproduces the mean state and seasonal variability of temperature, mixed layer depth, sea surface height, and phytoplankton (Appendix A).

3. Results

3.1. Subseasonal variability of satellite fields

3.1.1. Subseasonal contribution to total variance

In this section, we evaluate the importance of the subseasonal variability of chlorophyll (CHL), SST, and meridional wind stress (MWS),

as percentage of total variance, and identify the frequencies where that subseasonal variability is the strongest. Power spectra are computed from daily mean time series of CHL, SST, and MWS for regions SHR, R1 and R2 (shown in Fig. 1), with the Cooley-Tukey method (Cooley and Tukey, 1965), using a Bartlett window and non-overlapping band averaging with 12 degrees of freedom (Fig. 2). The subseasonal, intraseasonal and submonthly variances are obtained by integrating the power spectrum over the 5–130 day, 30–90 day, and 5–30 day bands, respectively. Table 2 shows the percentages of variance associated with each band, with the percentages of variance at annual and semi-annual frequencies given as a reference. The subseasonal variability of MWS, CHL, and SST is the largest in R2, representing 83%, 57%, and 27% of the total variance. SST displays greater onshore-offshore differences in the subseasonal contribution, which is about 3.5 times larger in the shelf regions than in SHR. The submonthly (higher frequency) contribution to the MWS in all three regions is much greater (61%) than it is to CHL (23–32%) and SST (3–10%). That is not the case for the intraseasonal band, which contributes to ca. 10–20% of the variance of MWS, CHL, and SST. Although the intraseasonal CHL variance does not represent the largest fraction of subseasonal variance (15% to 22%), significant subseasonal peaks are found in the intraseasonal band (Fig. 2b). Similarities among dominant intraseasonal frequencies of CHL (59, 50, and 43 days) and MWS (64, 50, 43) strongly suggest wind-driven variability of phytoplankton biomass within the intraseasonal band (Fig. 2a, b). Spectral SST peaks also show some correspondence with the MWS peaks, though only the 50-day SST peak in R2 is close to the 95% significance level (Fig. 2c).

Table 2
Percentage of total variance associated with the subseasonal (5–130 day), intraseasonal (30–90 days), submonthly (5–30 days), annual and semi-annual frequencies for meridional wind stress (MWS), SST, and chlorophyll (CHL) derived from satellite sensors for region SHR, R1 and R2 (Fig. 1).

	Region	5–130 d	30–90 d	5–30 d	Annual	Semi-annual
MWS	SHR	81	19	61	14	2
	R1	82	17	62	13	2
	R2	83	20	61	12	2
CHL	SHR	44	15	24	39	9
	R1	45	17	23	44	6
	R2	57	22	32	35	2
SST	SHR	7	3	3	89	2
	R1	24	12	9	59	5
	R2	27	15	10	61	1

3.1.2. Spatiotemporal patterns of subseasonal time series

The spectral analysis showed that an important fraction of variance in time series of MWS, SST, and CHL is within the subseasonal band. Now we examine the main spatiotemporal patterns associated with that subseasonal variability. To this effect, Empirical Orthogonal Function (EOF) decomposition (von Storch and Zwiers, 1999) of 5–

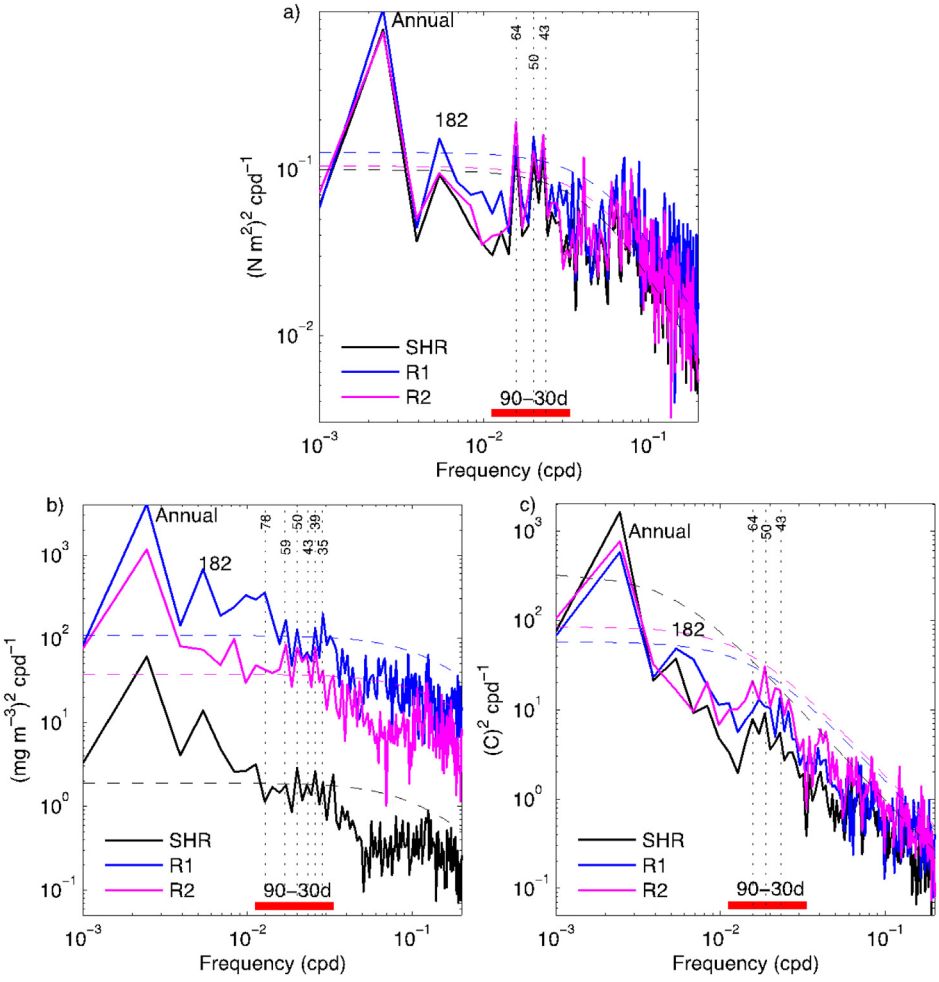

Fig. 2. Spectral analysis. Power spectra of the (a) Cross-Calibrated Multi-Platform meridional wind stress, (b) MODIS chlorophyll, and (c) SST derived from regions SHR, R1 and R2 shown in Fig. 1. Spectra are calculated using the Cooley-Tukey method with non-overlapping band averaging, considering 12 degrees of freedom (Cooley and Tukey, 1965). Black, blue, and magenta dashed lines show the 95% significance level for SHR, R1 and R2, respectively, estimated from red noise spectra. Vertical dotted lines and numbers (days) highlight frequencies with the largest intraseasonal peaks. Thick red horizontal bar depicts the intraseasonal (30–90 days) band. (For interpretation of the references to color in this figure legend, the reader is referred to the web version of this article.)

130 days band-pass Lanczos filtered (Duchon, 1979) time series of MWS, SST, and CHL are derived within the SHR. The spatial patterns from the two EOF modes are shown in Fig. 3. The first EOF (EOF1) mode explains 87%, 55%, and 21% of the MWS, SST, and CHL variability, respectively. The three EOF1 fields are positive over the whole domain, reflecting an alongshore coherence of the spatial pattern (Fig. 3a–c). The following specific features can be distinguished: 1) MWS has the largest anomalies between 36°–39°S, with a maximum (~0.1 N m^{-2}) 120 km northwest of Point Lavapie (37.2°S); 2) SST has the largest near-shore anomalies (~0.8 °C) at 37.2°–38.5°S and south of 39°S with a jet-like structure extending northward and detaching from Point Lavapie; 3) the largest anomalies of CHL occur onshore of the 200 m isobath (gray contour in Fig. 3c), most notably at 36°–37.2°S and 38.5°–40°S, where CHL anomalies exceed 0.5 mg m^{-3}. The second EOF (EOF2) explains 10%, 9%, and 10% of the MWS, SST, and CHL variability, respectively. This EOF2 mode represents a meridional dipole with zero amplitude near Point Lavapie (Fig. 3d–f). Although the first two EOF modes of CHL only account for 31% of the subseasonal variance, the explained variance is significantly larger over the shelf. Both EOFs together represent 40–50% of the subseasonal variability in the coastal regions over 36°–37.24°S and 38.5°–39.5°S (Fig. 3l).

Important differences exist between the first principal component (PC1) time series of MWS and the PC1 of both SST and CHL (Fig. 4a–c). The subseasonal signal of MWS has similar amplitude year-round, while the subseasonal signals of SST and CHL have strong seasonality, with the maximum amplitude occurring during spring-summer. Another difference among the PC1 time series is that MWS has much stronger submonthly variability than SST and CHL. Spectral analyses of the PC1 time series (not shown) indicate that 74% of the total PC1-MWS variance occurs at periods shorter than 30 days, while only 41% and 31% of the PC1-SST and PC1-CHL variance is associated with submonthly variability. Despite the important temporal and spectral differences between the PC1-MWS and both PC1-SST and PC1-CHL, the correlations among the time series are significant, being stronger in spring-summer than fall-winter (Table 3). The 30–90 day filtered PC1 (*f*PC1) time series show much stronger coherence over the intraseasonal band than at submonthly frequencies (Fig. 4d, e; Table 3). In both cases (PC1 and *f*PC1), the sign of the correlation is consistent with a modulation of the coastal phytoplankton biomass by wind-driven upwelling. The intraseasonal MWS leads the intraseasonal SST (CHL) by 5 (3) days during spring-summer. That CHL leads SST by roughly two days is unexpected for a coastal upwelling dynamic, as we would predict that wind-driven response in SST lead the response in CHL (e.g. Bane et al., 2007). This inconsistency in the lag might be associated with the interpolation used to fill cloud-obscured days, which precludes a finer estimation of the phase relationship among the MODIS-derived and QuikSCAT time series.

The *f*PC1 time series have significant interannual changes. Periods with strong intraseasonal variability occur during the spring-summer of 2005–2006 and 2006–2007, while relatively weak intraseasonal variability is observed during the spring-summer of 2007–2008 and 2010–2011. To evaluate further if interannual changes in the intraseasonal signals are consistent among MWS, SST, and CHL, we estimate the 18-month running average variance (RV) time series from the *f*PC1s. An 18-month running window was selected to filter out the annual variation in the *f*PC1 variance. The standardized RV time series of MWS, SST, and CHL reveal similar interannual fluctuations (Fig. 4f). The correlation coefficients are 0.61, 0.58, and 0.78 for MWS-SST, MWS-CHL, and SST-CHL, respectively. Weak intraseasonal variability prevails during 2004 and 2008, while strong intraseasonal variability prevails during

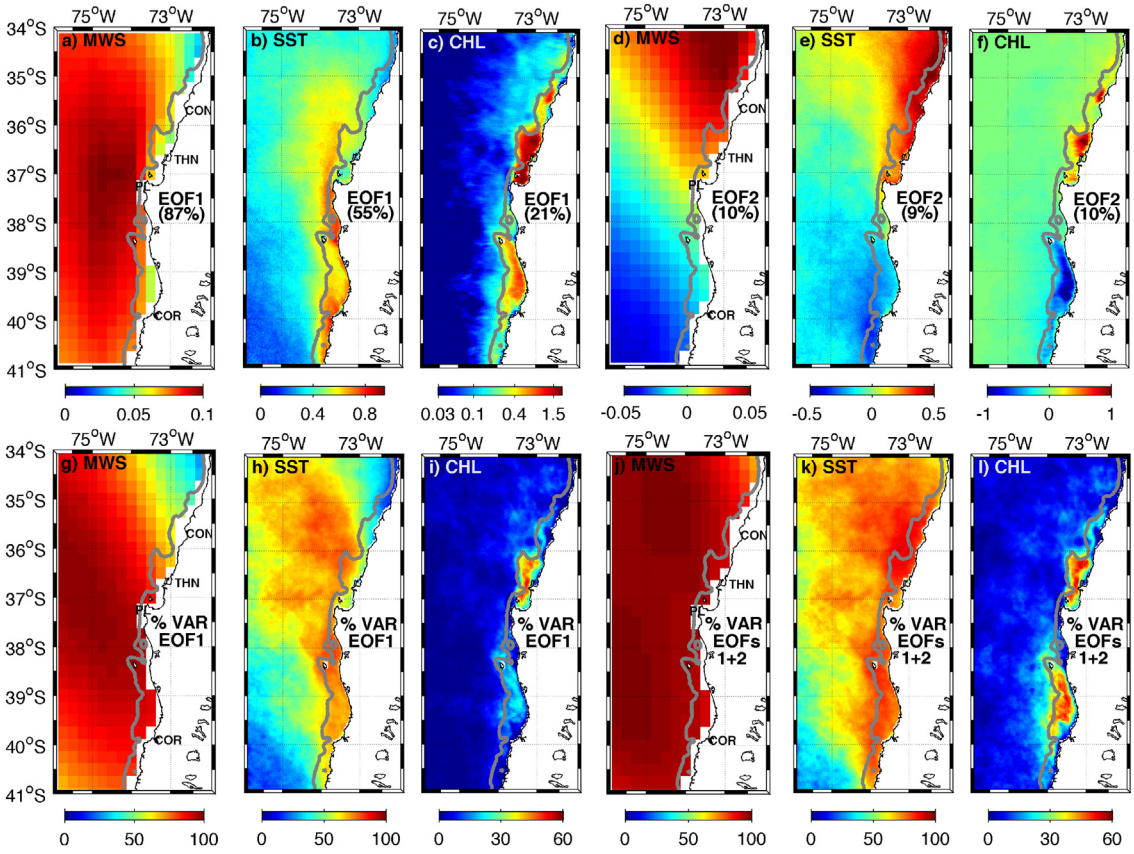

Fig. 3. EOF analysis of satellite data. (a–c) depict the first (EOF1) and (d–f) the second (EOF2) spatial patterns derived from 5 to 130 day band-pass filtered time series of the (a, d) satellite Cross-Calibrated Multi-Platform meridional wind stress (MWS), (b, e) MODIS SST, and (c, f) MODIS surface chlorophyll (CHL). EOF units of meridional wind stress, SST, and chlorophyll are N m^{-2}, °C, and mg m^{-3}, respectively. Lower panels (g–l) are the percentage of variance explained at each grid point by (g–i) EOF1 and (j–l) EOF1 + EOF2 combined for MWS, SST, and CHL. Gray contours depict the 200 m isobath.

2005–2006. The RV analysis suggests that interannual changes in the intraseasonal wind signal can modulate the intraseasonal variability of SST and CHL.

3.1.3. Intraseasonal variability and large-scale atmospheric disturbances

Previous studies off central Chile suggested that alongshore wind variability is influenced by Madden-Julian Oscillation (MJO) disturbances (e.g. Hormazabal et al., 2002; Rahn, 2012). Consequently, we examined whether interannual changes in the amplitude of the intraseasonal MWS signal respond to the intensity of the MJO. The Real-time Multivariate MJO time series 1 (RMM1), an index derived by Wheeler and Hendon (2004) from EOF decomposition of combined fields of equatorial zonal winds and outgoing long-wave radiation, was used as an index of MJO activity. A 30–90 day band-pass filter was applied to RMM1 to eliminate the minor fraction of variance not related to the intraseasonal band. The intraseasonally filtered time series of RMM1 and MWS are significantly correlated ($r = 0.40$, RMM1 leading by 4 days), illustrating consistent phase relationship over most of the period (Fig. 4g). However, the amplitude of the MWS anomalies is weakly related to the RMM1 amplitude, and the correlation between the 18-month running variance time series of MWS and RMM1 is not significant (not shown).

To describe the large-scale atmospheric pattern associated with the strongest intraseasonal anomalies of chlorophyll and MJO disturbances, composites of the mean intraseasonal anomalies of sea level pressure (SLP) and 200 hPa geopotential-height (200 gph) are derived (Fig. 5). The CHL composites correspond to the mean anomalies of SLP and 200 gph for the 10-day intervals preceding the peaks (amplitude > 1, high CHL composite) and troughs (amplitude < −1, low CHL composite) in the *f*PC1-CHL time series. The preceding 10-day interval was

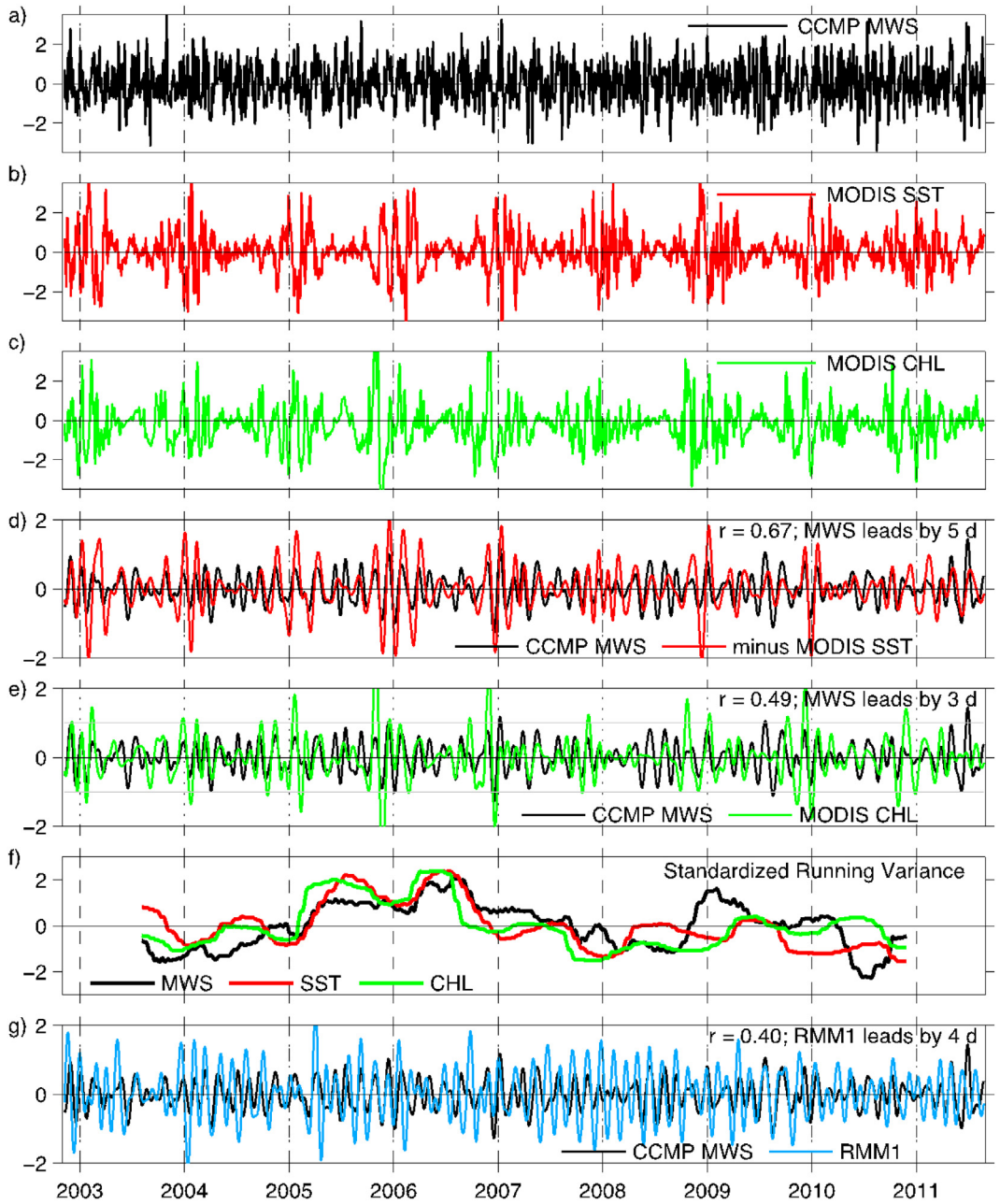

Fig. 4. PC1 time series of a) meridional wind stress (MWS), b) MODIS SST, and c) MODIS surface chlorophyll (CHL); d) 30–90 day band-pass filtered PC1 (*f*PC1) of MWS and minus MODIS SST (SST multiplied by −1); e) *f*PC1 time series of MWS and MODIS CHL; f) standardized 18-month running variance of the *f*PC1 time series of MWS, SST, and CHL; g) real-time multivariate MJO series 1 (RMM1; Wheeler and Hendon, 2004) and MWS. Ticks on the ordinate mark January 1st of each year.

Table 3
Maximum lagged correlation between the first principal component time series of meridional wind stress (MWS), SST, chlorophyll (CHL) and surface phytoplankton (PHY). PC1 is the first principal component mode, and *f*PC1 is the 30–90 day band pass filtered PC1 mode. The lag (days) at maximum correlation is indicated in parenthesis (negative values indicate the second time series lags the first).

	Time series	Variables	Overall[a]	Oct–Mar[a]	Apr–Sep[a]
Satellite	PC1	MWS – SST	−0.46 (−1)	−0.67 (−1)	−0.26 (−3)
		MWS – CHL	0.32 (0)	0.41 (0)	0.30 (0)
		SST – CHL	−0.39 (+2)	−0.46 (0)	
	*f*PC1	MWS –SST	−0.67 (−5)	−0.86 (−5)	−0.55 (−8)
		MWS – CHL	0.49 (−3)	0.68 (−3)	0.27 (−2)
		SST – CHL	−0.53 (+2)	−0.59 (+2)	
Model	PC1	MWS – SST	−0.59 (−2)	−0.69 (−2)	−0.50 (−2)
		MWS – PHY	0.45 (−6)	0.62 (−5)	0.28 (−8)
		SST – PHY	−0.82 (−2)	−0.90 (−3)	−0.56 (−4)
	*f*PC1	MWS –SST	−0.83 (−7)	−0.94 (−6)	−0.74 (−8)
		MWS – PHY	0.77 (−8)	0.93 (−8)	0.55 (−9)
		SST – PHY	−0.93 (−3)	−0.95 (−3)	−0.78 (−4)

[a] Only correlation coefficients significant at 99% confidence level are reported. Sample size in the significance test was obtained with the modified Chelton method to account for time series autocorrelation (Pyper and Peterman, 1998).

considered to account for the response lag between wind and chlorophyll. The MJO composites correspond to the mean anomalies of SLP and 200 gph during MJO phases 4–5 and 8–1 (Wheeler and Hendon, 2004). MJO phases 4–5 (8–1) are linked to deep convection over Indonesia (equatorial Pacific) and strong (weak) upwelling favorable winds off central Chile (Wheeler and Hendon, 2004; Rahn, 2012). The composites based on the *f*PC1-CHL time series (Fig. 5a, b) show a wave-like anomaly pattern with a zonal wave number 3. High CHL periods are associated with positive (anticyclonic) SLP and 200 gph anomalies at high latitudes centered around 10°E, 170°W, and 80°W (off southern Chile), and negative (cyclonic) SLP and 200 gph off the Amundsen and Ross seas (West Antarctic), and around 50°W and 50°E (Fig. 5a). The pattern is reversed during the low CHL periods (Fig. 5b). The spatial patterns in the high and low CHL composite are similar to the patterns associated with the MJO phases 4–5 and 8–1 (Fig. 5c, d), but the amplitude of the intraseasonal SLP and 200-gph anomalies in the CHL-based composite are larger. This strongly suggested that high-latitude atmospheric disturbances linked to the MJO influence the intraseasonal variability of phytoplankton biomass off central Chile.

3.2. Subseasonal variability of modeled surface fields

The first EOF of modeled SST and phytoplankton (PHY) explain 35% and 26% of the total subseasonal variance, respectively (Fig. 6a, b). The second EOF of model SST and PHY (not shown) have meridional dipoles with zero crossings near Point Lavapie, similar to those shown for satellite SST and CHL (Fig. 3e, f). Overall, the spatial patterns of EOF1 of the model (Fig. 6a, b) and satellite SST (Fig. 3b, c) are very similar, although the magnitude of the model SST anomalies is ~20% larger than the MODIS SST anomalies in the coastal region south of 37°S. The first EOFs of satellite CHL and model PHY are also similar, although the alongshore discontinuity in the EOF1-PHY anomalies over the coastal region near 37.5°S is not as pronounced as in the EOF1-CHL anomalies. The first EOF patterns of SST and PHY in the model are linked to the main spring-summer circulation (arrows in Fig. 6a, b), with the

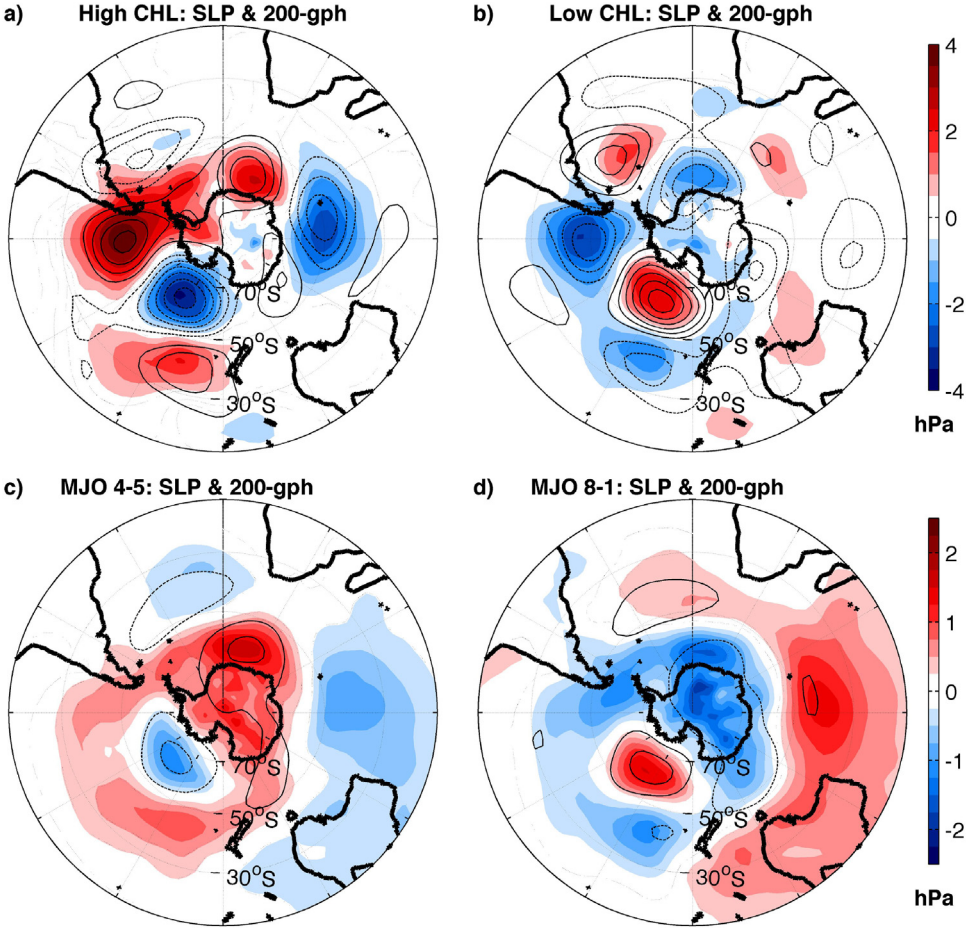

Fig. 5. Composite analysis. Intraseasonal anomalies of sea level pressure (SLP, background color) and 200 hPa geopotential height (200-gph, solid and dash contours for positive and negative anomalies (every 10 m), respectively) for periods preceding the CHL-*f*PC1 peaks >1 (a) and CHL-*f*PC1 troughs smaller than −1 (b), and for MJO phases 4–5 (c) and 8–1 (d). All composites are based on data from Oct.–Mar. SLP and 200-gph.

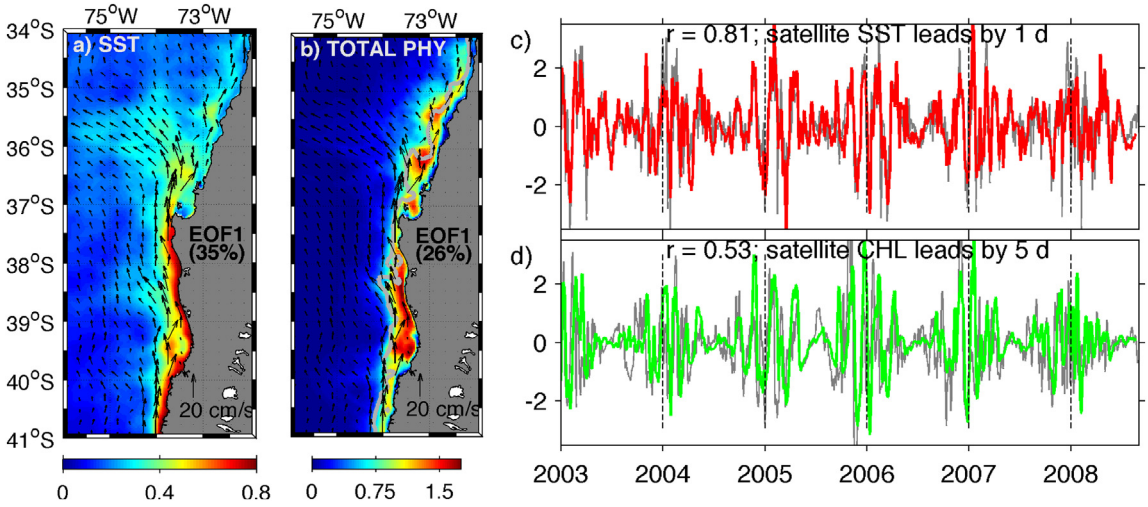

Fig. 6. EOF analysis of model outputs. The left two panels show the first EOF mode derived from the subseasonal time series of (a) modeled SST and (b) surface phytoplankton. The EOF units for SST and phytoplankton fields are °C and mmol N m^{-3}, respectively. Plotted on each panel is the model mean surface current during spring-summer. Panel (c) is the first principal component (PC1) time series of modeled SST (red) and satellite SST (gray). Panel (d) is the PC1 time series of modeled total surface phytoplankton (green) and satellite chlorophyll (gray). The correlation coefficient (r) between time series in panels c and d is indicated. (For interpretation of the references to color in this figure legend, the reader is referred to the web version of this article.)

strongest SST and PHY anomalies located onshore of a strong equatorward coastal jet that develops south of 37°S. The jet detaches from the coast near Point Lavapie, a feature that is well represented by the first EOF of both the model and satellite SST. High PHY anomalies develop where the current is weaker, which allows for a longer residence time of the water and growth and accumulation of phytoplankton.

The PC1 series from the modeled SST and PHY (Fig. 6c, d) reproduce the dominant temporal fluctuations of the satellite PC1 time series, especially the 30–90 day variability. The correlation between the PC1 time series of satellite and model SST is 0.81 (satellite SST leading by 1 day), and the correlation between the PC1 of satellite CHL and model PHY is 0.53 (CHL leading by 5 days). The correlation between MWS and model SST and PHY show maximum values during spring-summer (Oct-Mar), similar to the correlations derived from satellite data (Table 3). The *f*PC1 time series of MWS, modeled SST and PHY are highly correlated, suggesting a strong response of the coastal circulation and ecosystem to the intraseasonal variability of the wind. During spring-summer, *f*PC1-MWS leads *f*PC1-SST (PHY) by 6 (8) days. The 2-day lead of the *f*PC1-SST compared to *f*PC1-PHY is to be expected in an upwelling system.

3.3. Plankton vertical distribution and composition

Intraseasonal wind oscillations not only influence the spatial pattern of surface phytoplankton, they also impact the vertical distribution and composition of the plankton community. To illustrate this, we examined the model outputs in two coastal regions (R1 and R2, north and south of Pt. Lavapie, respectively; locations shown in Fig. 1), during the spring-summer of 2005–2006 (Fig. 7). Four strong intraseasonal wind oscillations significantly disturb the vertical distribution of temperature and plankton during that season. Differences in the mean and vertical structure of temperature and plankton are evident between regions, as upwelling favorable winds are stronger in R1. However, some similar plankton patterns can be identified in both regions. Diatom biomass peaks at 0–10 m about 7–10 days after the wind maxima, following the surface increase in NO_3 concentrations (not shown) and surface temperature decline (Fig. 7c, d). On the other hand, subsurface maxima (at ~10–30 m) of small phytoplankton tend to develop during upwelling relaxation/downwelling periods, a few days after the wind stress minima (Fig. 7g, h). Microzooplankton biomass responds to the changes in diatom and small phytoplankton biomass, with subsurface peaks during upwelling relaxation/downwelling (Fig. 7i, j). Mesozooplankton biomass shows similar fluctuation as microzooplankton biomass, lagging the diatom peak by about two weeks (Fig. 7k, l).

Interannual changes in the amplitude of the intraseasonal MWS can create significant differences in plankton composition. To visualize this, we compare plankton compositions during the spring-summer of 2005–2006 and 2007–2008, which have strong and weak intraseasonal wind oscillations, respectively (Fig. 8a, b). The time series in Fig. 8c–f correspond to vertically averaged plankton concentrations over the upper 60 m (or bottom when bottom depth is shallower than 60 m) in region R2. The subseasonal wind oscillations determine significant fluctuations in diatom and mesozooplankton biomass during both periods (Fig. 8c, d). Fluctuations in small phytoplankton and microzooplankton are also observed, but the amplitude of the changes is one order of magnitude smaller than in diatom and mesozooplankton (Fig. 8e, f). Thus, variations in the diatom to total phytoplankton ratio (PL:P), as well as the mesozooplankton to total zooplankton ratio (ZL:Z), are mainly determined by changes in the large plankton components (Fig. 8g, h). The strong intraseasonal wind fluctuation during 2005–2006 determines changes in the plankton ratios (Fig. 8g) with PL:P exceeding 0.8 shortly after the peaks in upwelling, and declining to <0.65 shortly after relaxation/downwelling periods. Similarly, ZL:Z exhibits intraseasonal changes ranging from 0.63 to 0.82, lagging by ~2 weeks the changes in PL:P (Fig. 8g). On the other hand, the weak intraseasonal wind signal during 2007–2008 determines small changes in plankton composition, mainly due to submonthly variability (Fig. 8h). PL:P remains >0.8 from mid November to late January, smoothly declining during Feb-Apr as upwelling favorable winds decline. ZL:Z is around 0.75, showing weak submonthly changes.

3.4. Seasonal modulation of the intraseasonal signal

To understand the underlying dynamics that lead to seasonal modulation of phytoplankton biomass at the subseasonal band, we examined nutrient and light limitation of phytoplankton growth using time-depth growth limitation factor diagrams for region R2 during 2005–2007. Growth limitation factors vary between 0 and 1, with 1 indicating no-limitation and 0 meaning no-growth. The temporal variability of the nutrient limitation factor (NLF) (Fig. 9b) closely resembles the fluctuations in MWS (Fig. 9a), showing a strong seasonal cycle with maximum values (i.e. weak growth limitation) during strong upwelling winds. The light limitation factor (LLF) also shows strong seasonality (Fig. 9c), modulated by the annual cycle in solar radiation (Fig. 9a). Minimum

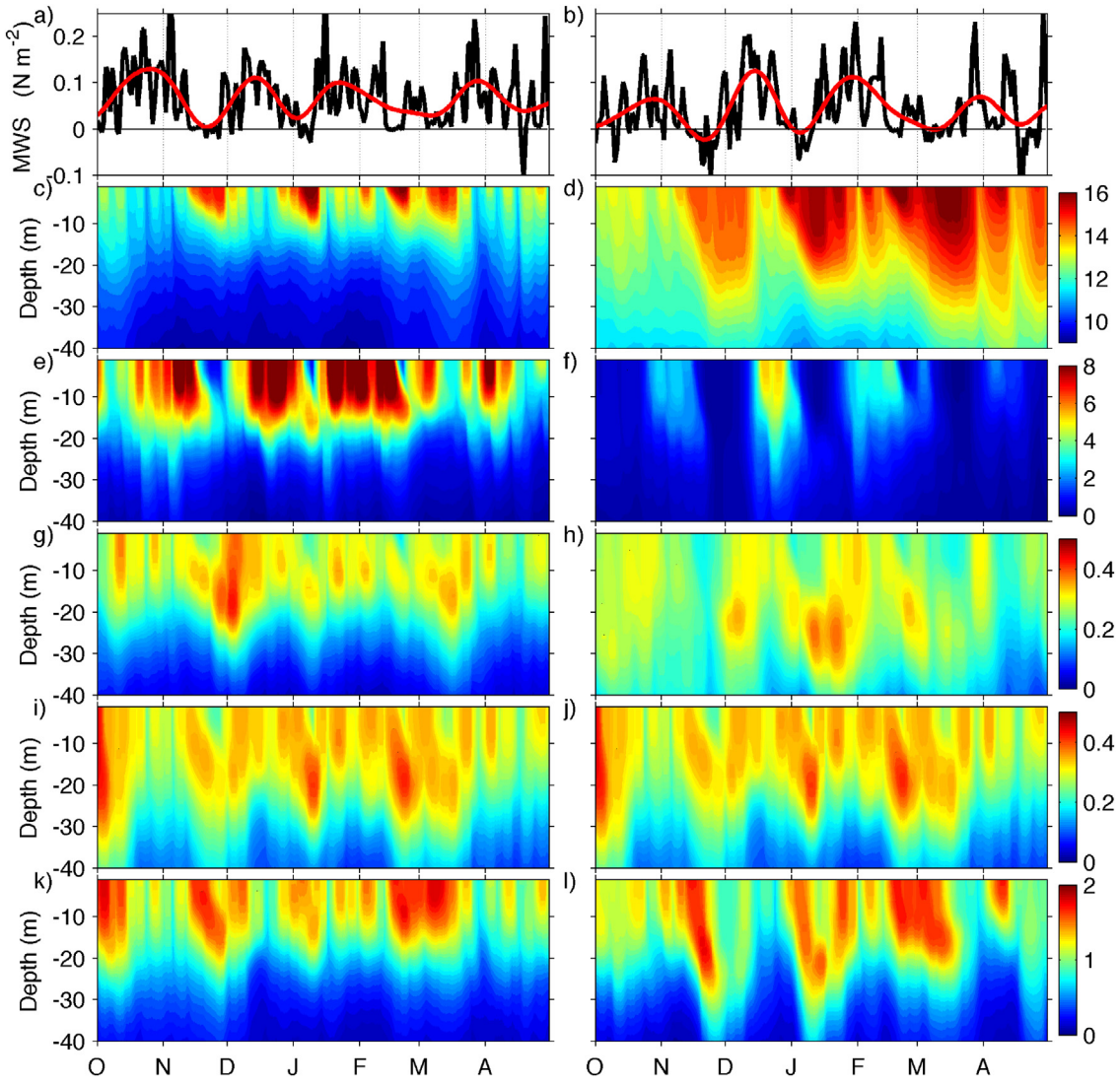

Fig. 7. Impact of the intraseasonal wind variability in regions R1 (left) and R2 (right) (regions shown in Fig. 1) during spring-summer of 2005–2006: (a, b) Daily (black) and 30-day low-pass filtered (red) time series of meridional wind stress, (c, d) temperature (°C), (e, f) diatom, (g, h) small phytoplankton, (i, j) microzooplankton, and (k, l) mesozooplankton biomass. Biomass is in units of mmol N m^{-3}. (For interpretation of the references to color in this figure legend, the reader is referred to the web version of this article.)

LLF values (i.e. strong light limitation) occur during winter, when solar radiation is minimum and the MLD is deeper (black contour in Fig. 9d) due to downwelling winds (Fig. 9a). Intraseasonal wind oscillations can produce strong intraseasonal changes in NLF during fall-winter (like in 2007). However, the changes in NLF during fall-winter weakly impact diatom biomass (Fig. 9d), which is more strongly limited by light. Another potential factor influencing the seasonal modulation of the intraseasonal diatom variability is temperature since the phytoplankton growth rate depends upon the ambient temperature in our biochemical model (Eppley, 1972; Table 1). The temperature dependent effect is maximum near the surface (0–20 m) from November to April (Fig. 9e). However, the mean effect of temperature in that layer during Nov–Apr is only 4% larger than in May–Oct (2.40 and 2.32, respectively). Moreover, the temperature tends to reduce the amplitude of the intraseasonal diatom biomass oscillations, as the upwelling nutrient-rich waters that trigger the diatom bloom during spring-summer are colder than the downwelling nutrient depleted waters.

4. Discussion

Previous studies of subseasonal variability in eastern boundary current systems have been based on 25-km resolution satellite microwave SSTs (Renault et al., 2009; Dewitte et al., 2011; Goubanova et al., 2013; Illig et al., 2014). However, microwave sensors cannot detect SSTs within 50 to 75 km of the coast due to the land's influence on microwave emissions. In this study, subseasonal variability of physical and ecological properties were examined using 1 km resolution MODIS SST and chlorophyll data capable of resolving patterns along the narrow (10–80 km wide) continental shelf off central Chile. Additionally, a coupled physical-biochemical model facilitated examination of subseasonal variability of the depth dependent planktonic ecosystem, which is not observable by satellite. Model and satellite-derived SST and surface phytoplankton/chlorophyll patterns agree well. We obtained consistent and similar patterns of intraseasonal variability from two independent sources, satellite data and model outputs, which provides added confidence that our analysis of upwelling dynamics off central Chile is robust. However, upwelling strength (Appendix A) in the nearshore region is overestimated in the model, possibly due to inaccurate (too high) wind forcing in the coastal zone where the estimated winds (Section 2.2) do not properly resolve the coastal wind drop-off (Renault et al., 2012). This lack of wind drop-off at the coast overestimates the coastal wind intensity and coastal upwelling to about 25 km offshore. On the contrary, the consequent underestimation of the cyclonic wind stress curl (curl is zero nearshore) translates in decreased Ekman pumping

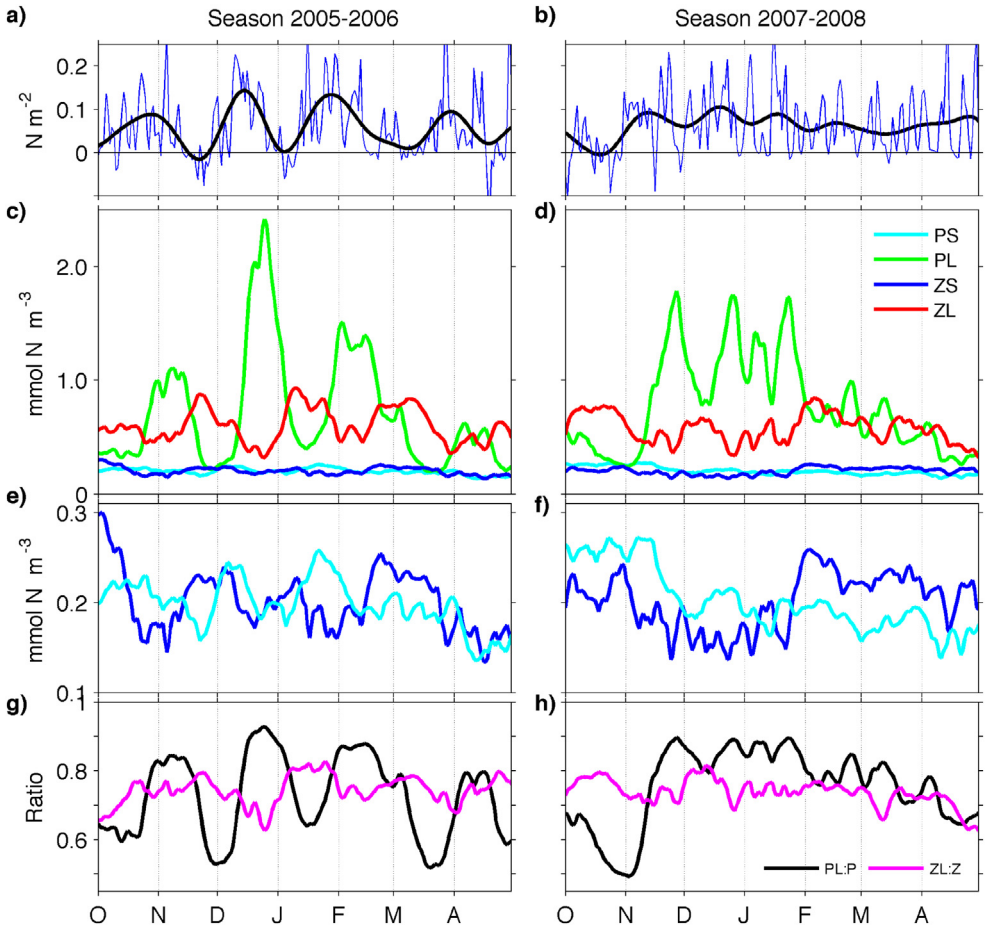

Fig. 8. Plankton fluctuations during spring-summer season of 2005–2006 (left) and 2007–2008 (right): (a, b) daily (thin line) and 30-day low-pass filtered (thick line) time series of meridional wind stress for region R2 shown in Fig. 1; (c, d) plankton concentration averaged over the upper 60 m within region R2. Cyan, green, blue, and red lines correspond to small phytoplankton (PS), diatom (PL), microzooplankton (ZS), and mesozooplankton (ZL), respectively. (e-f) as in (c-d) but for PS and ZS only. (g-h) Concentration ratio between PL and total phytoplankton (PL:P, black) and between ZL and total zooplankton (ZL:Z, magenta). (For interpretation of the references to color in this figure legend, the reader is referred to the web version of this article.)

and Sverdrup poleward flow (Albert et al., 2010; Astudillo et al., 2017). Thus, a compensating effect could exist between enhanced coastal upwelling and decreased Ekman pumping, which may help to reduce the nearshore (0–25 km) upwelling bias (Astudillo et al., 2017). Improved representation of coastal wind in regional ocean models will be required to simulate better the effect of coastal upwelling and Ekman pumping on coastal circulation and plankton dynamics.

4.1. EOF patterns

The spatial structure of the first EOF mode derived from the subseasonal time series (5–130 day band-pass filtered series) of MWS resembles spatial anomalies related to the atmospheric coastal jet (Garreaud and Munoz, 2005; Renault et al., 2009), an intermittent mesoscale feature, roughly 400 km wide and 1000 km long, characterized by surface equatorward winds > 10 m s^{-1}. The subseasonal variability of this atmospheric jet drives significant changes in coastal upwelling and ocean mixing, such that the strongest EOF1-SST anomalies (south of Point Lavapie) are concurrent with the strongest nearshore anomalies of MWS. The largest subseasonal anomalies of chlorophyll and phytoplankton, however, are not co-located with the strongest SST anomalies. The coastal jet has a major role in the spatial configuration of SST and CHL/PHY anomalies. The largest model PHY and satellite CHL anomalies are inshore of the coastal jet, in regions that favor coastal retention and long residence times. The second EOF mode of the subseasonal time series of MWS, SST, and CHL display meridional dipoles with zero values near Point Lavapie. This spatial configuration can be associated with a poleward progressing pattern, which is evident in time-latitude diagrams of MWS, SST, and CHL from the shelf region (not shown). The pattern is consistent with the results of Rahn (2012), see his Fig. 5), who identified a poleward progression in the wind and sea level pressure anomalies based on the MJO phases.

Examination of the 30–90 day band-pass filtered PC1 (*f*PC1) time series of MWS, satellite and model SST, CHL, and PHY reveals a strong response of the SST and phytoplankton to intraseasonal wind oscillations. Sustained upwelling favorable winds imply a sustained supply of nutrients that support high phytoplankton production and increasing zooplankton biomass (Bane et al., 2007). During spring-summer, when the coupling between MWS and SST is the strongest, the *f*PC1 series of satellite SST and model SST lag *f*PC1-MWS by 5 and 6 days, respectively. The MWS-SST lags are similar to the lags derived from observational studies in the Oregon coastal upwelling system (3 days) (Bane et al., 2007) and Benguela Current (7 days) (Goubanova et al., 2013), and a modeling study off Peru (8 days) (Illig et al., 2014). CHL and PHY off Chile lag MWS by 3 and 8 days, respectively. The discrepancy between correlation lags derived from satellite chlorophyll and modeled surface phytoplankton may result from missing MODIS data interpolated by DINEOF being unable of capturing the peak of the bloom. The MWS-PHY lag off Chile is similar to the lag between wind stress and model chlorophyll off Oregon (7.4 days; Bane et al., 2007), although they obtained a much longer lag, 13.6 days, between coastal wind stress and

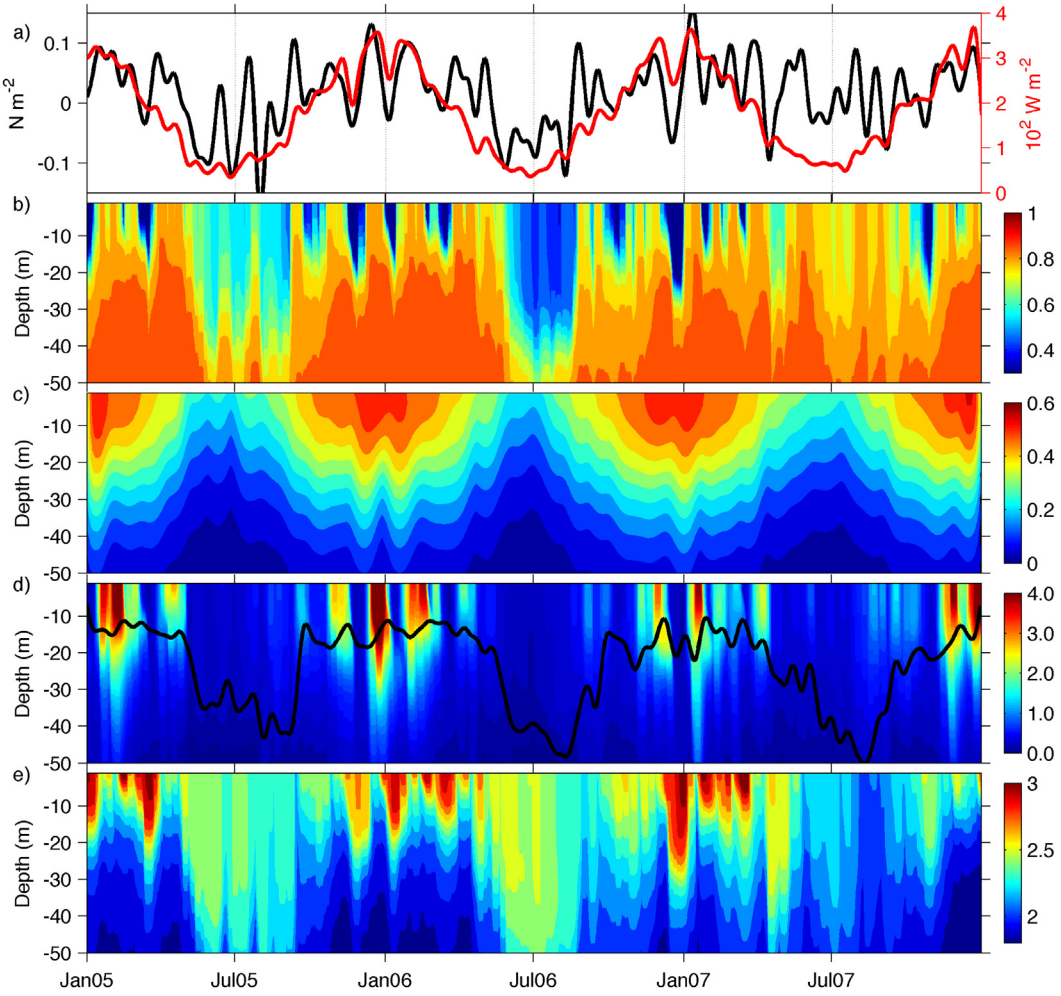

Fig. 9. January 2005 to December 2007 seasonal modulation of phytoplankton-growth within region R2 (depicted in Fig. 1): a) low-pass series of wind stress (black) and surface shortwave radiation (red); b) modeled nutrient limitation factor (unitless (0–1); see text); c) modeled light limitation factor (unitless (0–1); see text); d) diatom concentration (mmol N m^{-3}); e) temperature dependent factor for diatom growth (unitless, equivalent to $e^{0.0693 * \text{temperature}}$). Black contour in panel (d) depicts the mixed layer depth. (For interpretation of the references to color in this figure legend, the reader is referred to the web version of this article.)

chlorophyll at a coastal mooring located 20 km offshore at the edge of the coastal upwelling front.

4.2. Seasonal modulation of the intraseasonal signal

Phytoplankton biomass, measured as satellite chlorophyll and modeled phytoplankton, has similar subseasonal variability as SST, showing the largest subseasonal anomalies during spring-summer. In the central Benguela and northern Humboldt systems (Goubanova et al., 2013; Illig et al., 2014), seasonal differences in upper ocean stratification (vertical temperature gradient and mixed layer depth), explained the different subseasonal responses observed in spring-summer vs. fall-winter, with winds providing a greater ocean response when the mixed layer was shallow. The seasonal variability of the MWS-SST correlation, observed previously for central Chile by Renault et al. (2009), is consistent with changes in our modeled mixed layer depth (MLD), which is deeper than 40 m in winter and about 15 m in summer (black contour in Fig. 9d). Our model results also suggest that the seasonal changes in the amplitude of the intraseasonal signal are mainly controlled by light limitation. This is consistent with results from Echevin et al. (2008), who concluded that one of the main processes affecting chlorophyll variability off Peru is the seasonal variation in solar radiation and MLD. Minimum chlorophyll concentration during winter off Peru is concurrent with the strongest upwelling favorable winds.

4.3. Large-scale atmospheric anomalies

The wind-driven intraseasonal variability of phytoplankton biomass appeared to be linked to high-latitude anomalies of sea level pressure (SLP) and the 200 hPa geopotential height (200 gph) (Fig. 5a, b). The patterns of SLP and 200 gph for the CHL composites are similar to the patterns associated with MJO disturbances. Positive SLP and 200 gph anomalies off southern Chile, and negative SLP and 200 gph off the Amundsen and Ross seas, are associated with the high CHL and MJO phases 4–5 composites. The anomalies are reversed in the low CHL and MJO phases 8–1 composites. Interestingly, the spatial pattern for the high CHL and MJO phases 4–5 composites resemble atmospheric anomalies associated with La Nina, while the low CHL and MJO phases 8–1 composites resemble anomalies associated with El Nino (Montecinos and Aceituno, 2003). This suggests that similar dynamics modulate local winds at the interannual (El Nino/La Nina) and intraseasonal timescales. According to Montecinos and Aceituno (2003), the mechanism responsible for the negative MWS anomalies off central Chile during El Nino, and resulting decrease in coastal upwelling, is an equatorward shift of the mid-latitude storm track, linked to increasing blocking activity at high latitudes (seen as positive SLP off the Amundsen and Ross Sea; Fig. 5b). On the other hand, positive MWS anomalies and increased upwelling during La Nina are associated with a poleward shift of the mid-latitude storm-track due to weak high-latitude blocking activity.

The link between the equatorial variability associated with MJO and the high latitude atmospheric disturbances derived from the composite analysis may be related to the Pacific-South America (PSA) teleconnection pattern (Ghil and Mo, 1991). The PSA is an eastward propagating atmospheric wave train with zonal wave number 3, triggered by anomalous deep convection over the equatorial Pacific linked to MJO, which influences blocking activity at high latitude (Rutllant and Fuenzalida, 1991; Mo and Paegle, 2001). Since the PSA pattern is modulated by MJO disturbances, the intraseasonal upwelling anomalies could potentially be predicted, with a lead-time of 2–3 weeks.

4.4. Plankton vertical distribution and composition

Diatom concentrations are maxima near the surface during strong upwelling periods, but small phytoplankton tend to have subsurface maxima during relaxation/downwelling periods, when the vertical stratification is the strongest (Figs. 7). Those subsurface maxima can have a vertical extent < 10 m and are located 15 to 30 m deep. As a consequence, satellite chlorophyll sensors may not detect them (Kemp and Villareal, 2013), or significantly underestimate coastal phytoplankton biomass during upwelling relaxations. As r-selected opportunistic species (Falkowski and Oliver, 2007), diatoms respond strongly to the nutrient increases during strong upwelling periods, producing large amplitude intraseasonal changes in near-surface phytoplankton biomass, especially during spring-summer. This is congruous with the conceptual framework of phytoplankton mandala (Margalef, 1997), which links phytoplankton succession to nutrient supply and turbulence. The estimated contribution of diatom to phytoplankton ratio (PL:P), as well as mesozooplankton to zooplankton (ZL:Z), are similar to values reported in observational studies on the shelf (e.g. Anabalon et al., 2007). The influence of small phytoplankton and microzooplankton on the PL:P and ZL:Z ratios is small, consistent with observational studies showing minor changes in the biomass of autotrophic flagellates and heterotrophic protists (Bottjer and Morales, 2007).

Interannual variability in the intraseasonal wind anomalies produces important differences in plankton structure, which is evident in the comparison between the spring-summer seasons of 2005–2006 and 2007–2008 (Fig. 8). Submonthly changes dominate during 2007–2008, but intense intraseasonal wind fluctuations occur during 2005–2006, configuring distinct scenarios in term of plankton composition. Diatom biomass dominated over most of the spring-summer of 2007–2008, but it was strongly depressed during the extended upwelling relaxation periods of 2005–2006. We modeled relatively simple changes in plankton structure involving four plankton functional groups. However, we expect that intraseasonal upwelling changes may trigger more complex plankton responses. Indeed, Gonzalez et al. (2015), using monthly observations of copepods from a coastal station near Concepcion (~36.8°S) during spring-summer, found distinct differences in copepod assemblages between upwelling and relaxation periods. Their results also suggested an increase in copepod diversity linked to enhanced stratification.

4.5. Implications for higher trophic levels

Intraseasonal wind variability, by creating periods with alternating high and low phytoplankton abundance, could impact higher trophic levels, including commercially important small pelagic fish, such as common sardine and anchovy. Because both common sardine and anchovy have extended, multi-month spawning seasons, the survival of early life stages may be affected by the spatiotemporal coupling/uncoupling between feeding larvae and larval prey availability (abundance and type) that is determined by the patterns of wind forcing. The interannual timing of the first strong intraseasonal peak of phytoplankton biomass in spring (seen in the *f*PC1 time series of CHL) varies from September to November (Fig. 4e), and might impact annual recruitment of common sardine, which is linked to spring phytoplankton production (Gomez et al., 2012). In addition, wind-driven changes in the upper layer temperature will affect biological rates, modulating the egg and larval development durations of these fish. The impact of intraseasonal upwelling variability on larval development may be complex, as the positive effect on growth associated with abundant planktonic food due to upwelling may be offset by slower development and growth due to colder temperatures. The coupling between small pelagic fish spawning intensity and intraseasonal upwelling oscillations also requires further examination, since reproductive traits (fecundity, egg size) of adult females appear to respond quickly (on order of weeks) to environmental factors (Claramunt et al., 2012). Finally, the intraseasonal wind variability could have a significant impact on dispersion and connectivity patterns between sites of adult spawning and sites of juvenile recruitment. The potential impacts of the intraseasonal variability on larval fish survival and recruitment, growth, fecundity and connectivity suggest that intraseasonal upwelling variability should be considered when examining the dynamics of higher trophic levels.

Acknowledgements

F.G. is very grateful for the support of the Chilean National Commission for Scientific and Technological Research (CONICYT), the Fulbright Student Program, and the Oregon State University Graduate School and College of Earth, Ocean, and Atmospheric Sciences. We also thank JAMSTEC and AVISO for kindly providing OFES model outputs and altimetry data, respectively. We thank the two anonymous reviewers for their useful comments that greatly improved the original manuscript version.

Appendix A. Supplementary data

Supplementary data to this article can be found online at http://dx.doi.org/10.1016/j.jmarsys.2017.05.003.

References

Albert, A., Echevin, V., Lévy, M., Aumont, O., 2010. Impact of nearshore wind stress curl on coastal circulation and primary productivity in the Peru upwelling system. J. Geophys. Res. Oceans 115 (C12).

Anabalon, V., Morales, C.E., Escribano, H.R., Varas, M.A., 2007. The contribution of nano- and micro-planktonic assemblages in the surface layer (0–30 m) under different hydrographic conditions in the upwelling area off Concepcion, central Chile. Prog. Oceanogr. 75, 396–414.

Astudillo, O., Dewitte, B., Mallet, M., Frappart, F., Rutllant, J.A., Ramos, M., Bravo, L., Goubanova, K., Illig, S., 2017. Surface winds off Peru-Chile: observing closer to the coast from radar altimetry. Remote Sens. Environ. 191, 179–196.

Atlas, R., Hoffman, R.N., Ardizzone, J., Leidner, S.M., Jusem, J.C., Smith, D.K., Gombos, D., 2011. A cross-calibrated, multiplatform ocean surface wind velocity product for meteorological and oceanographic applications. Bull. Am. Meteorol. Soc. 92:157–174. http://dx.doi.org/10.1175/2010BAMS2946.1.

Bane, J.M., Spitz, Y.H., Letelier, R.M., Peterson, W.T., 2007. Jet stream intraseasonal oscillations drive dominant ecosystem variations in Oregon's summertime coastal upwelling system. PNAS 104 (33), 13262–13267.

Beckers, J.M., Rixen, M., 2003. EOF calculations and data filling from incomplete oceanographic datasets. J. Atmos. Ocean. Technol. 20 (12), 1839–1856.

Belmadani, A., Echevin, V., Dewitte, B., Colas, F., 2012. Equatorially-forced intraseasonal propagations along the Peru-Chile coast and their relation with the nearshore eddy activity in 1992–2000: a modelling study. J. Geophys. Res. http://dx.doi.org/10.1029/2011JC007848.

Bonhomme, C., Aumont, O., Echevin, V., 2007. Advective transport caused by intraseasonal Rossby waves: a key player of the high chlorophyll variability off the Peru upwelling region. J. Geophys. Res. 112, C09018. http://dx.doi.org/10.1029/2006JC004022.

Botsford, L.W., Lawrence, C.A., Dever, E.P., Hastings, A., Largier, J., 2006. Effect of variable winds on biological productivity on continental shelves in coastal upwelling systems. Deep-Sea Res. II 53, 3116–3140.

Bottjer, D., Morales, C.E., 2007. Nanoplanktonic assemblages in the upwelling area off Concepcion (36°S), central Chile: abundance, biomass, and grazing potential during the annual cycle. Prog. Oceanogr. 75, 415–434.

Breaker, L., Liu, P., Torrence, C., 2001. Intraseasonal oscillations in sea surface temperature, wind stress, and sea level off the central California coast. Cont. Shelf Res. 21 (2001), 727–750.

Carton, J., Giese, B., 2008. A reanalysis of ocean climate using simple ocean data assimilation (SODA). Mon. Weather Rev. 136 (8), 2999–3017.

Chapman, D.C., 1985. Numerical treatment of cross-shelf open boundaries in a barotropic coastal ocean model. J. Phys. Oceanogr. 15, 1060–1075.
Chenillat, F., Riviere, P., Capet, X., Franks, P.J.S., Blanke, B., 2013. California coastal upwelling onset variability: cross-shore and bottom-up propagation in the planktonic ecosystem. PLoS ONE 8 (5), e62281. http://dx.doi.org/10.1371/journal.pone.0062281.
Claramunt, G., Castro, L.R., Cubillos, L.A., Hirche, H.J., Perez, G., Braun, M., 2012. Inter-annual reproductive trait variation and spawning habitat preferences of *Engraulis ringens* off northern Chile. Rev. Biol. Mar. Oceanogr. 47, 227–243.
Cooley, J.W., Tukey, J.W., 1965. An algorithm for the machine calculation of complex Fourier series. Math. Comput. 19 (90), 297–301.
Correa-Ramirez, M.A., Hormazabal, S.E., Morales, C.E., 2012. Spatial patterns of annual and interannual surface chlorophyll-a variability in the Peru–Chile Current System. Prog. Oceanogr 92, 8–17.
Cushing, D.H., 1990. Plankton production and year-class strength in fish populations; an update of the match/mismatch hypothesis. Adv. Mar. Biol. 26, 249–293.
Dee, D.P., et al., 2011. The ERA-interim reanalysis: configuration and performance of the data assimilation system. Q. J. R. Meteorol. Soc. 137:553–597. http://dx.doi.org/10.1002/qj.828.
Dewitte, B., Illig, S., Renault, L., Goubanova, K., Takahashi, K., Gushchina, D., Mosquera, K., Purca, S., 2011. Modes of covariability between sea surface temperature and wind stress intraseasonal anomalies along the coast of Peru from satellite observations (2000–2008). J. Geophys. Res. Oceans 1978–2012 (116), C4.
Duchon, C., 1979. Lanczos filtering in one and two dimensions. J. Appl. Meteorol. 18, 1016–1022.
Echevin, V., Aumont, O., Ledesma, J., Flores, G., 2008. The seasonal cycle of surface chlorophyll in the Peruvian upwelling system: a modelling study. Prog. Oceanogr. 79, 167–176.
Echevin, V., Aurelie, A., Marina, L., Michelle, G., Olivier, A., Alice, P., Gilles, G., 2014. Intraseasonal variability of nearshore productivity in the Northern Humboldt Current System: the role of coastal trapped waves. Cont. Shelf Res. 73, 14–30.
Eppley, R.W., 1972. Temperature and phytoplankton growth in the sea. Fish. Bull. 70, 1063–1085.
Escribano, R., Hidalgo, P., González, H., Giesecke, R., Riquelme-Bugueño, R., Manríquez, K., 2007. Seasonal and inter-annual variation of mesozooplankton in the coastal upwelling zone off central-southern Chile. Prog. Oceanogr 75 (3), 470–485.
Falkowski, P.G., Oliver, M.J., 2007. Mix and match: how climate selects phytoplankton. Nat. Rev. Microbiol. 5 (10), 813–819.
Fischer, G., Karakas, G., 2009. Sinking rates and ballast composition of particles in the Atlantic Ocean: implications for the organic carbon fluxes to the deep ocean. Biogeosciences 6, 85–105.
Flather, R.A., 1976. A tidal model of the northwest European continental shelf. Mem. Soc. R. Sci. Liege 6, 141–164.
Galperin, B., Kantha, L.H., Hassid, S., Rosati, A., 1988. A quasi-equilibrium turbulent energy model for geophysical flows. J. Atmos. Sci. 45, 55–62.
Garreaud, R., Munoz, R., 2005. The low-level jet off the subtropical west coast of South America: structure and variability. Mon. Weather Rev. 133, 2246–2261.
Ghil, M., Mo, K., 1991. Intraseasonal oscillations in the global atmosphere, part 1, southern hemisphere. J. Atmos. Sci. 48, 780–790.
Gomez, F., Montecinos, A., Hormazabal, S., Cubillos, L.A., Correa-Ramirez, M.A., Chavez, F.P., 2012. Impact of spring upwelling variability off southern-central Chile on common sardine (*Strangomera bentincki*) recruitment. Fish. Oceanogr. 21:405–414. http://dx.doi.org/10.1111/j.1365-2419.2012.00632.x.
Gonzalez, C.E., Escribano, R., Hidalgo, P., 2015. Intra-seasonal variation of upwelling and its effects on copepod community structure off central/southern Chile (2002–2009). Hydrology 758 (1), 61–74.
Goubanova, K., Illig, S., Machu, E., Garçon, V., Dewitte, B., 2013. SST subseasonal variability in the central Benguela upwelling system as inferred from satellite observations (1999–2009). J. Geophys. Res. Oceans 118:4092–4110. http://dx.doi.org/10.1002/jgrc.20287.
Hormazabal, S., Shaffer, G., Letelier, J., Ulloa, O., 2001. Local and remote forcing of sea surface temperature in the coastal upwelling system off Chile. J. Geophys. Res. 106, 16,657–16,671.
Hormazabal, S., Shaffer, G., Pizarro, O., 2002. Tropical Pacific control of intraseasonal oscillations off Chile by way of oceanic and atmospheric pathways. Geophys. Res. Lett. 29 (6). http://dx.doi.org/10.1029/2001GL013481.
Illig, S., Dewitte, B., Goubanova, K., Cambon, G., Boucharel, J., Monetti, F., Romero, C., Purca, S., Flores, R., 2014. Forcing mechanisms of intraseasonal SST variability off central Peru in 2000–2008. J. Geophys. Res. Oceans 119:3548–3573. http://dx.doi.org/10.1002/2013JC009779.
Kemp, A.E.S., Villareal, T.A., 2013. High diatom production and export in stratified waters – a potential negative feedback to global warming. Prog. Oceanogr. 119, 4–23.
Kishi, M., Kashiwai, M., Ware, D., Megrey, B., Eslinger, D., et al., 2007. NEMURO - a lower trophic level model for the North Pacific marine ecosystem. Ecol. Model. 202 (1–2), 12–25.
Large, W.G., Pond, S., 1981. Open ocean momentum flux measurements in moderate to strong winds. J. Phys. Oceanogr. 11, 324–336.
Li, Q.P., Franks, P.J.S., Landry, M.R., Goericke, R., Taylor, A.G., 2010. Modeling phytoplankton growth rates and chlorophyll to carbon ratios in California coastal and pelagic ecosystems. J. Geophys. Res. 115 (G4), 1–12.
Madden, R.A., Julian, P.R., 1972. Description of global-scale circulation cells in the Tropics with a 40–50 day period. J. Atmos. Sci. 29, 1109–1123.
Marchesiello, P., McWilliams, J., Shchepetkin, A., 2001. Open boundary conditions for long-term integration of regional oceanic models. Ocean Model 3:1–20. http://dx.doi.org/10.1016/S1463-5003(00)00013-5.
Margalef, R., 1997. Our biosphere. In: Kinne, O. (Ed.), Excellence in Ecology. Ecology Institute, Oldendorf/Luhe.
Masumoto, Y., Sasaki, H., Kagimoto, T., Komori, N., Ishida, A., et al., 2004. A fifty year eddy-resolving simulation of the world ocean: preliminary outcomes of OFES (OGCM for the Earth Simulator). J. Earth Simul. 1 (April), 35–56.
Mo, W.K., Paegle, J.N., 2001. The Pacific-South Atlantic modes and their downstream effects. J. Climatol. 21, 1211–1229.
Montecinos, A., Aceituno, P., 2003. Seasonality of the ENSO related rainfall variability in central Chile and associated circulation anomalies. J. Clim. 16, 281–296.
Morales, C.E., Hormazabal, S., Andrade, I., Correa-Ramirez, M.A., 2013. Time-space variability of chlorophyll-a and associated physical variables within the region off Central-Southern Chile. Remote Sens. 5, 5550–5571.
Platt, T., Gallegos, C.L., Harrison, W.G., 1980. Photoinhibition of photosynthesis in natural assemblages of marine phytoplankton. J. Mar. Res. 38, 687–701.
Pyper, B.J., Peterman, R.M., 1998. Comparison of methods to account for autocorrelation in correlation analyses of fish data. Can. J. Fish. Aquat. Sci. 55, 2127–2140.
Rahn, D.A., 2012. Influence of large scale oscillations on upwelling-favorable coastal wind off central Chile. J. Geophys. Res. Atmos. 117 (D19), 1–11.
Renault, L., Dewitte, B., Falvey, M., Garreaud, R., Echevin, V., Bonjean, F., 2009. Impact of atmospheric coastal jet off central Chile on sea surface temperature from satellite observations (2000–2007). J. Geophys. Res. 114, C08006. http://dx.doi.org/10.1029/2008JC005083.
Renault, L., Dewitte, B., Marchesiello, P., Illig, S., Echevin, V., Cambon, G., Ramos, M., Astudillo, O., Minnis, P., Ayers, J.K., 2012. Upwelling response to atmospheric coastal jets off central Chile: a modeling study of the October 2000 event. J. Geophys. Res. 117, C02030. http://dx.doi.org/10.1029/2011JC007446.
Rose, K., Megrey, B., Werner, F., Ware, D., 2007. Calibration of the NEMURO nutrient–phytoplankton–zooplankton food web model to a coastal ecosystem: Evaluation of an automated calibration approach. Ecol. Model. 202 (1–2), 38–51.
Rutllant, J., Fuenzalida, H., 1991. Synoptic aspects of the central Chile rainfall variability associated with the Southern Oscillation. Int. J. Climatol. 11, 63–76.
Rutllant, J.A., Rosenbluth, B., Hormazabal, S., 2004. Intraseasonal variability of wind-forced coastal upwelling off central Chile (30_S). Cont. Shelf Res. 24:789–804. http://dx.doi.org/10.1016/j.csr.2004.02.004.
Shaffer, G., Hormazabal, S., Pizarro, O., Salinas, S., 1999. Seasonal and interannual variability of currents and temperature over the slope off central Chile. J. Geophys. Res. 104, 29,951–29,961.
Shchepetkin, A., McWilliams, J., 2005. The regional oceanic modeling system (ROMS): a split-explicit, free-surface, topography-following coordinate oceanic model. Ocean Model 9:347–404. http://dx.doi.org/10.1016/j. ocemod.2004.08.002.
Smith, W., Sandwell, D., 1997. Global seafloor topography from satellite altimetry and ship depth soundings. Science 277:1956–1962. http://dx.doi.org/10.1126/science.277.5334.1956.
Song, Y., Haidvogel, D.B., 1994. A semi-implicit ocean circulation model using a generalized topography-following coordinate system. J. Comput. Phys. 115 (1), 228–244.
Spitz, Y.H., Newberger, P.A., Allen, J.S., 2003. Ecosystem response to upwelling off the Oregon coast: behavior of three nitrogen-based models. J. Geophys. Res. 108. http://dx.doi.org/10.1029/2001JC001181.
von Storch, H., Zwiers, F.W., 1999. Statistical Analysis in Climate Research. 484 pp. Cambridge Univ. Press, Cambridge, U. K.
Tapia, F., Castro, L., Daneri, G., Fernandez, C., González, H., Hidalgo, P., Morales, C.E., Pizarro, O., 2010. FIP Technical Report 2008-20. University of Concepcion (165 pp. plus appendix (in Spanish)).
Wheeler, M.C., Hendon, H.H., 2004. An all-season real-time multivariate MJO index: development of an index for monitoring and prediction. Mon. Weather Rev. 132: 1917–1932. http://dx.doi.org/10.1175/1520-0493(2004) 132<1917:AARMMI>2.0.CO;2.
Yoshie, N., Yamanaka, Y., Rose, K.A., Eslinger, D.L., Ware, D.M., Kishi, M.J., 2007. Parameter sensitivity study of a lower trophic level marine ecosystem model "NEMURO". Ecol. Model. 202, 26–37.